Research Article Vol. 33, No. 20 / 6 Oct 2025 / Optics Express 41522
Optics EXPRESS

Revealing the influence of solvent polarity and refractive index on whispering gallery mode-based laser sensors

JIANWEI LI,[1,†] DONGYANG LI,[1,†] GUOCHENG FANG,[2,†] CHENGDE GUO,[1] NINGYUAN NIE,[2] XIYU SUN,[2] XIAOYUN PU,[1] YINGXIA JIN,[3] YU-CHENG CHEN,[2,4] AND YUANXIAN ZHANG[1,2,5]

[1]School of Physics and Astronomy, Yunnan University, Kunming 650091, China
[2]School of Electrical and Electronics Engineering, Nanyang Technological University, Singapore
[3]School of Materials and Energy, Yunnan University, Kunming 650091, China
[4]yucchen@ntu.edu.sg
[5]zyx74635@163.com
[†]These authors contributed equally to this work.

Abstract: Whispering-gallery-mode (WGM) lasers are highly sensitive sensing tools in solution-based environments, but their performance is influenced by multiple factors, leading to complex spectral shifts. In this study, we decode the influence of solvent polarity on the WGM laser sensors, exploring its interaction with solvent refractive index (RI) in optofluidic systems. A binary polarity solvent of ethanol (EtOH) and ethylene glycol (EG) containing rhodamine 6G (Rh6G) is utilized as the lasing gain medium. Experimental results indicate that increasing solvent polarity induces a redshift in the lasing wavelength, while rising RI lowers the quality factor (Q-factor), causing a competing blueshift. These opposing effects collectively impact the overall performance of the sensors. Based on these observations, we propose a predictive framework for optimizing WGM laser sensors across different Q-factor levels, offering valuable insights for sensor design and fabrication.

1. Introduction

Whispering-gallery-mode (WGM) optofluidic laser sensors represent a cutting-edge technology, merging microlaser techniques with microfluidics to enable highly sensitive, non-invasive, compact, and adaptable sensing platforms [1–4]. These sensors are widely employed to detect a broad range of physical, chemical, and biological targets, including proteins, RNA, DNA, viruses, specific ions, and more [5–13].

The sensitivity of WGM optofluidic laser sensors is influenced not only by the intrinsic properties of the resonator, such as the quality factor (Q-factor) which determines the cavity's ability to confine light [14,15], but also by various external factors. These include temperature fluctuations [16–18], pH variations [19–21], changes in solvent refractive index (RI) [22,23], and notably, the polarity of the solvent environment. When the sensor is influenced by multiple factors simultaneously, its overall sensitivity may increase or decrease compared to the effect of a single parameter. Therefore, in practical sensing applications, it is crucial to thoroughly evaluate how these variables impact the performance of WGM laser sensors to ensure adaptability across diverse conditions. However, most previous studies have predominantly concentrated on the isolated effects of individual parameters (such as temperature, pH, and RI) on the sensitivity of WGM sensor, while often neglecting the combined influences among them. In particular, the effect of solvent polarity on WGM sensors has been largely unexplored, despite its significant impact on the photophysical properties of the gain medium, including absorption, and emission behavior. Given the complexity of real-world sensing environments, multiple parameters often

#568769 https://doi.org/10.1364/OE.568769
Journal © 2025 Received 23 May 2025; revised 7 Sep 2025; accepted 8 Sep 2025; published 22 Sep 2025

Optics EXPRESS

fluctuate simultaneously. Therefore, considering variations in only a single factor during the sensor design may yield inaccurate or even misleading outcomes.

Among these parameters, solvent polarity and RI variations are particularly variable during measurements [22,24]. In this paper, we employ a fiber optofluidic laser (FOFL) to explore how solvent polarity and RI collectively influence the behavior of WGM lasing. Figure 1 presents an overview of the lasing generation and sensing mechanism, *i.e.*, Fig. 1(a) schematically depicts a bare quartz optical fiber (without cladding) with a uniform RI of 1.458, integrated within a microfluidic channel and axially pumped to induce WGM lasing. Figure 1(b) and (d) conceptually show how solvent polarity and RI influence the performance of the WGM sensor system; Fig. 1(c) depicts the lasing spectral shifts that result from these two factors. Specifically, alterations in solvent polarity affect the energy gap between the ground and excited states of the solute molecules, thereby changing the resonance wavelength of the resonator. Meanwhile, changes in solvent RI alter the evanescent wave (EW) penetration depth and the Q-factor of the resonator, leading to a shift in the lasing wavelength. Our experimental results reveal that increasing solvent polarity induces a redshift in the lasing wavelength, while rising solvent RI reduces the Q-factor of the resonator, causing a blueshift. These opposing effects interact to shape the overall sensing performance of the FOFL sensors. Based on these findings, we propose a framework for evaluating WGM optofluidic laser sensors' sensitivity across different Q-factor levels, providing insights for designing sensors suited to various conditions.

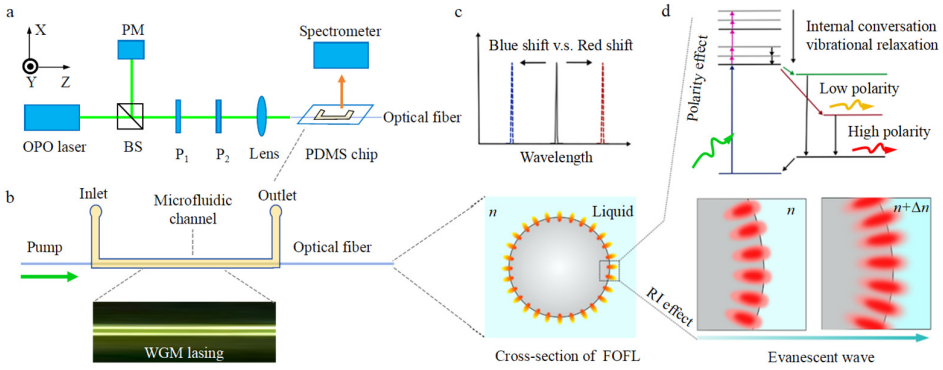

Fig. 1. (a) Schematic diagram of the experimental setup. P_1 and P_2: polarizers; BS: beam splitter; PM: power meter. (b) Schematic of the FOFL system illustrating the process of pumping, lasing, and sensing. The lower inset illustrates the WGM lasing emission in operation, while the right inset presents a cross-sectional view of the FOFL, which is used to demonstrate the principle of the WGM lasing generation and sensing. (c) Spectral wavelength shifts of WGM lasing induced by changes in solvent polarity and RI. (d) Effects of solvent polarity and RI on the performance of a WGM optofluidic laser system.

2. Experimental section

2.1. Experimental setup

Figure 1(a) presents the schematic of the experimental setup. More details are available in our previous report [10,11]. Briefly, a bare quartz optical fiber (RI = n_1 = 1.458, diameter (D) = 125 μm), functioning as both the optical resonator and sensing reactor, is embedded within a polydimethylsiloxane (PDMS, RI = 1.405) microchannel. The lengths of the microfluidic channel and the optical fiber are 5 mm and 4 cm, respectively. Rh6G dye molecules are dissolved in a mixed polarity solution of ethanol (EtOH, low RI and polarity) and ethylene glycol (EG, high RI and polarity), which serves as the gain cladding medium for the optical fiber. By adjusting the

Optics EXPRESS

EtOH to EG volume ratio, the RI (n_2) of the binary solution can be varied from 1.361(EtOH) to 1.432(EG), and the polarity (permittivity (ε)) from ~25 to 40. The fiber is longitudinally pumped by an optical parametric oscillator (OPO) laser at 532 nm (5 ns pulse width and 20 Hz repetition rate). Since the RI of the optical fiber is higher than that of the surrounding cladding solution, the beam propagates along the fiber axis via total internal reflection (TIR) at the fiber-cladding interface. The evanescent field of the pump light extends beyond the fiber surface, effectively exciting dye molecules located within the evanescent region of the WGMs of the ring resonators. This excitation subsequently facilitates lasing emission supported by the WGMs [25,26]. The lasing emission is collected by a multimode fiber oriented perpendicular to the Z-axis and directed to a spectrometer equipped with an ICCD detector (PI-Max 1024RB), offering a spectral resolution of 0.05 nm when using a 2400 g/mm grating. During the experiment, the desired pump energy is controlled by adjusting the polarization directions of polarizers P_1 and P_2. Figure 1(b) presents an enlarged view of the PDMS chip from Fig. 1(a), which is used to demonstrate the principles of pumping, lasing, and sensing in a FOFL system, along with key factors such as solvent polarity and RI that may affect WGM lasing behavior. Compared to transverse pump, this longitudinal pump configuration provides a more uniform excitation field (as shown in the lower inset of Fig. 1(b)), effectively suppressing background noise and thereby enhancing the signal-to-noise ratio of sensing [25,26]. The right inset of Fig. 1(b) shows a cross-section of the fiber within a microfluidic channel, which is utilized to illustrate the mechanisms of WGM lasing generation and sensing. Figure 1(c) describes the lasing spectral wavelength shifts originated from the variation in the solvent polarity and RI. Figure 1(d) schematically presents the influence of solvent polarity and RI on WGM lasing. On one hand, changes in solvent polarity alter the energy gap between the ground and excited states of the dye molecules, leading to a shift in the lasing wavelength. On the other hand, variations in the solvent RI affect the penetration depth of the evanescent field into the cladding solution, which also results in a wavelength shift. In the experiment, the Rh6G is maintained at a concentration of 2 mM. All measurements are conducted at room temperature (25 °C).

2.2. Materials

Quartz optical fiber (Transmittance per meter > 99%) was purchased from Nanjing Chunhui Science and Technology Industrial Co., Ltd. (China). The fiber consists of a high-refractive-index silica glass core and a low-refractive-index polymer cladding. The polydimethylsiloxane (PDMS, RI = 1.405) microfluidic channel, was provided by HICOMP Microtech (Suzhou) Co., Ltd. (China). Rh6G (molecular weight 479.02 g mol^{-1}, CAS Number 989-38-8, Sigma-Aldrich), sodium dodecyl sulfate (SDS) (molecular weight 288.38 g mol^{-1}, CAS Number 151-21-3, Sigma-Aldrich) surfactant. Other reagents, including $CaCl_2$, EtOH, and EG, were at least of analytical reagent grade unless specified. Deionized (DI) water was obtained using an ultrapure system (EU-LS-100TJ, China). All the reagents were used as received without further purification.

2.3. Sample preparation

Optical fibers with core diameters of 100, 125, 200, and 400 μm were all custom-fabricated. Prior to use, the fibers were briefly exposed to a flame to remove the outer low-refractive-index polymer cladding. They were then immersed in 1% hydrofluoric acid (HF) solution for approximately 5 minute to obtain bare silica fibers with a uniform refractive index of 1.458. For the fiber with a diameter of 49 μm required in the experiment, no commercial customization was available. Instead, it was prepared by etching a 100 μm fiber in 1% HF solution for 24 hours. To prevent scattering loss from the optical fiber surface during lasing, all optical fibers were pre-cleaned in 1% HF solution for approximately 3 minutes. The stock solution was prepared by dissolving weighed amounts of Rh6G dye molecules in EtOH, and EG, respectively. In the experiment, the concentration of Rh6G was fixed at 2 mM. By adjusting the EtOH to EG volume ratio, the

Optics EXPRESS

RI (n_2) of the binary solution can be varied from 1.361(EtOH) to 1.432(EG), and the polarity (permittivity ε) from ~25 to 40. We also prepared a 2 mM Rh6G aqueous solution and adjusted its RI by adding $CaCl_2$ to the DI water containing 20 mM SDS surfactant. Permittivity ε of the binary solution is calculated by $\varepsilon^{1/3} = \varepsilon_1^{1/3} V_1/(V_1 + V_2) + \varepsilon_2^{1/3} V_2/(V_1 + V_2)\varepsilon^{1/3}$ were the permittivity (volume) of EtOH and EG, respectively. The RI of the solution was measured using an Abbe refractometer (2WAJ, Shanghai Csoif Co., Ltd. (China)).

3. Results and discussion

3.1. Absorption and emission properties of Rh6G in a binary solvent system

We initially employ a fiber with a diameter ($n_1 = 1.458$) of 125 μm to assess the photophysical properties of rhodamine 6G (Rh6G) with varying RI (n_2) in an EtOH and EG mixed polarity solution. Figure 2(a) displays the normalized absorption (fluorescence) spectra for different n_2. As n_2 increases from 1.361(EtOH) to 1.432 (EG), the absorption (emission) peak wavelength redshifts from 529.2 (564.2) nm to 533.4 (568.0) nm. Figure 2(b) depicts the relationship between the emission peak wavelength and n_2. A linear regression, represented by the black line, is performed over the n_2 range of 1.361 to 1.432. The results demonstrate that the fluorescence peak shift is directly proportional to n_2, exhibiting a sensitivity (slope) of approximately 56 nm/RIU and a correlation coefficient (R^2) of 0.9933.

3.2. Lasing emission properties

Subsequently, we investigate the lasing spectral response of the FOFL with solvent polarity and n_2. EtOH ($n_2 = 1.361$) is first selected as the solvent of Rh6G to analyze the WGM lasing emission behavior. Figure 2(c) shows the dependence of lasing emission intensity on pump energy density (PED), measured with a 150 g/mm grating, indicating a lasing threshold of 0.62 μJ/mm^2. The inset in Fig. 2(c) presents high-resolution laser spectra recorded using a 1200 g/mm grating at PED values of 3.0 μJ/mm^2 and 0.7 μJ/mm^2, respectively. The measured average mode spacing $\Delta\lambda$ ~0.57 nm between adjacent sharp peaks, which is consistent with the theoretical WGM mode spacing $\sim\lambda^2/(2\pi n_1 a)$, where λ (564.5 nm) the lasing central wavelength, n_1 (1.458) the RI of the fiber, and a (62.5 μm) the fiber radius, respectively. Polarization analysis further indicates that the observed lasing spectrum corresponds to a typical transverse electric (TE)-mode WGM lasing [11].

Figure 2(d) presents the lasing spectra varying with n_2 at a constant pump energy density (PED) of 6 μJ/mm^2, showing that the lasing central wavelength initially undergoes a redshift (1.361 to 1.400), followed by a blueshift (1.400 to 1.417). Additionally, when n_2 surpasses 1.417, the associated energy losses become excessively high, making it unfeasible to maintain the lasing threshold and consequently inhibiting the lasing emission. We also measure the lasing spectra with respect to n_2 for fiber diameters of 49, 100, 200, and 400 μm, respectively. During the measurements, the PED is maintained at 8 μJ/mm^2, and the corresponding lasing spectra are depicted in Fig. S1 (Supplement 1). Then, the correlation between the lasing central wavelength and n_2 has been established, as illustrated in Fig. 2(e). The lasing wavelength variations for the 100 and 200 μm fibers are similar to the 125 μm fiber. Specifically, as n_2 increases, the lasing central wavelength shows a distinct inflection point (IP). Before the IP, the wavelength experiences a rapid-to-slow nonlinear redshift. Beyond the IP, it presents a nonlinear accelerated blueshift in the opposite direction. The IPs occur at $n_2 = 1.395$, 1.400, and 1.410, corresponding to fiber diameters of 100, 125, and 200 μm, respectively. However, for fibers with the smallest diameter (*i.e.*, 49 μm), only a nonlinear accelerated blue shift is observed, while the largest diameter fiber (*i.e.*, 400 μm) displays a nonlinear decelerated redshift.

Optics EXPRESS

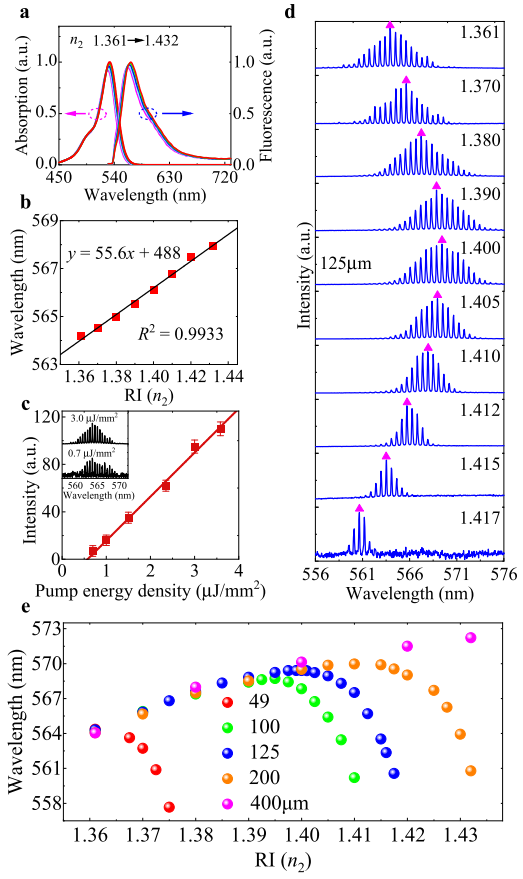

Fig. 2. Photophysical properties of Rh6G in an EtOH and EG mixed polarity solution. (a) Normalized absorption (emission) spectra vary with n_2. (b) The emission peak wavelength versus n_2. (c) Lasing peak intensity varied with pump energy density, with a lasing threshold of 0.62 μJ/mm^2. Error bars represent the standard deviation of five repeated measurements. The inset shows the lasing spectrum recorded with a 1200 g/mm grating. (d) Lasing spectra (D = 125 μm) varied with n_2. The magenta triangles indicate the position of the WGM selected to monitor the spectral shifting of the lasing emission. (e) The dependent of lasing central wavelength on n_2 at various optical fiber diameters.

Next, we conduct a comprehensive analysis of the individual and combined effects of solvent effects and RI-induced Q-factors on the lasing emission properties. Furthermore, we demonstrate how these factors collectively impact the overall sensing performance of the FOFL sensors.

3.3. *Effects of solvent polarity*

Generally, the wavelength redshift induced by the solvent polarity is typically regarded as a general solvent effect [27]. Particularly, the polar hydroxyl (-OH) group within a solvent molecule is recognized as an autochrome group, due to non-bonding electrons on the oxygen (O) atom. Although these non-bonding electrons do not generate distinct absorption peaks, they can induce a redshift in the wavelength of the chromophore when conjugated with it. As shown in Fig. 3(a), EtOH contains one -OH group and is less polar (permittivity $\varepsilon = 24.43$), while EG has two -OH groups and is more polar ($\varepsilon = 40.75$) [28]. Consequently, as n_2 increases from 1.361 to 1.432, the polarity of the solvent correspondingly increases, leading to an increase of non-bonding electrons.

Optics EXPRESS

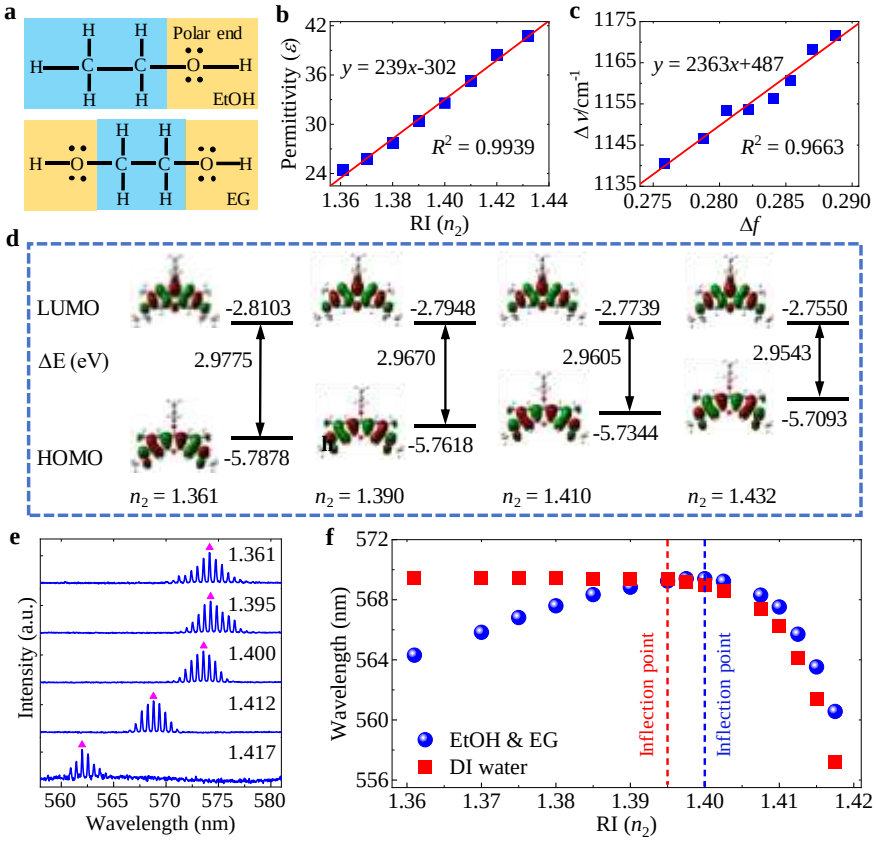

Fig. 3. (a) Electronic forms for EtOH and EG, the yellow rectangular boxes and black dots corresponding to the polar group (-OH) of the molecules and the non-bonding electrons on the oxygen atom, respectively. (b) permittivity (ε) of the polarity solvent as a function of n_2. (c) Lippert-Mataga plot for Rh6G across various n_2. (d) Electron cloud distribution of Rh6G in the HOMO and LUMO at different n_2 levels, calculated using Gaussian 09. (e) Lasing spectra of a 125 μm diameter fiber varied with n_2 in $CaCl_2$ aqueous solution. The magenta triangle marks the lasing central wavelength shift with n_2. (f) Comparison of the lasing central wavelength in $CaCl_2$ aqueous solution and EtOH & EG binary solution, respectively.

When these non-bonding electrons are connected with the solute molecules Rh6G, the energy gap (ΔE) between the ground state and excited states during the π→π* transition of the Rh6G system narrows, resulting in the redshift of the wavelength.

To quantitatively describe the polar-dependent spectral redshift, we have analyzed the photophysical properties of Rh6G with respect to n_2, as detailed in Table 1. The results indicate a strong positive correlation ($R^2 = 0.9939$) between solvent polarity and n_2, as illustrated in Fig. 3(b). Table 1 also summarizes the absorption and emission peaks, as well as Stokes shift ($\Delta\nu = \nu_{abs} - \nu_{em}$) of Rh6G varied with n_2. The Stokes shifts induced by changes in the solvent polarity can be regarded as an indication of the variation in dipole moment between the ground and excited states, which can be quantitatively described by the Lippert–Mataga equation [29]

$$\Delta\nu = \nu_{abs} - \nu_{em} = \frac{2}{hc}\Delta f \frac{(\mu_{ex} - \mu_g)^2}{a^3} + \text{constant}, \quad (1)$$

Optics EXPRESS

$$\Delta f = \frac{\varepsilon + 1}{\varepsilon - 1} - \frac{n_2^2 + 1}{n_2^2 - 1}, \tag{2}$$

where μ_{ex} and μ_g the dipole moments of the excited and ground states, respectively. h the Planck constant, c the speed of light, and a the Onsager radius of the solute, which can be derived from Avogadro number (N), molecular weight (M), and molecular density (d). The orientation polarizability Δf is a function of ε and n_2 of the solvent.

Table 1. Photophysical properties of Rh6G varied with n_2 of EtOH and EG binary solution

n_2	ε	λ_{abs}/nm	ν_{abs}/cm^{-1}	λ_e/nm	ν_e/cm^{-1}	$\Delta\nu$/cm^{-1}	Δf
1.361	24.43[27]	529.2	18896.4	564.2	17724.7	1171.7	0.28875
1.370	25.58	529.6	18882.2	564.5	17714.0	1168.2	0.28678
1.380	27.26	530.2	18860.8	564.9	17700.1	1160.7	0.28491
1.390	29.71	530.8	18839.5	565.5	17683.2	1156.3	0.28356
1.400	31.89	531.4	18818.2	566.1	17664.6	1153.6	0.28173
1.410	34.69	532.0	18797.0	566.8	17643.5	1153.5	0.28012
1.420	38.07	532.8	18768.7	567.5	17622.2	1146.5	0.27860
1.432	40.75[28]	533.4	18747.7	568.0	17607.2	1140.5	0.27586

The variation in the dipole moment ($\Delta\mu = \mu_{ex}$ - μ_g) can be estimated from the slope of the correlation between $\Delta\nu$ and Δf. Figure 3(c) presents the linear regression analysis of the Lippert-Mataga plot across various solvents, which shows a slope of 2363 cm^{-1} ($R^2 = 0.9663$) and a $\Delta\mu$ change of ~4.83 D. This suggests that increase solvent polarity can decrease the energy gap (ΔE) between the ground and the excited states of Rh6G, thereby causing a redshift in the wavelength.

To further investigate the impact of solvent polarity on the electronic energy levels of Rh6G, density functional theory (DFT) calculations are also conducted using the CAM-B3LYP/6-31G function with a Gaussian 09 software package. Figure 3(d) illustrates the distribution of electron clouds in the highest occupied molecular orbital (HOMO) and the lowest unoccupied molecular orbital (LUMO) of Rh6G, as well as the variation of electron energy levels (ΔE (eV)) with the solvent polarity. Obviously, the ΔE between LUMO and HOMO decreases with increasing RI (solvent polarity), supporting the observed redshift in wavelength.

To further confirm the redshift in the lasing wavelength due to the polar-induced solvent effect of EtOH and EG binary solution, we conduct a comparative experiment with a 125 μm fiber. The RI of the single solvent (aqueous solution) is adjusted by adding $CaCl_2$ to a SDS (20 mM) deionized (DI) water solution. As indicated by the magenta triangle in Fig. 3(e), the lasing central wavelengths remain stable within the n_2 range of 1.361 to 1.395. However, a noticeable blueshift occurs when n_2 exceeds 1.395. Figure 3(f) presents a comparative analysis of lasing central wavelengths observed in these two different solvents. Due to the absence of polar-induced solvent effects in DI water, three distinct features are observed in the lasing wavelength. Firstly, the IP ($n_2 = 1.395$) in DI water (red dashed line in Fig. 3(f)) appears earlier than in EtOH and EG solution ($n_2 = 1.400$, blue dashed line in Fig. 3(f)). Secondly, before the IP, the central wavelength stays nearly constant without redshift as n_2 increases. Additionally, the higher polarity ($\varepsilon \sim 80$) of water relative to the EtOH and EG mixed solution results in a longer lasing wavelength [30]. Thirdly, after the IP, the central wavelength shifts more rapidly to blue, indicating higher RI sensing sensitivity. Obviously, using a single solvent can significantly eliminate polar-induced solvent effects, thereby improving the sensing sensitivity.

Optics EXPRESS

3.4. Effects of RI-induced Q-factor

To illustrate the experimental observations of lasing wavelength shifts in various RI environments, we conduct a theoretical analysis using a 125 μm fiber in this section (Fig. 4). In a WGM-based FOFL, variations in the liquid RI around the resonator can substantially alter the EW penetration depth and the Q factors, leading to shifts in the wavelength. The penetration depth is directly proportional to the modal volume ratio (η) and can be quantitatively assessed using this ratio. Figures 4(a)-(f) depict these distributions of n_2 at 1.361, 1.405, and 1.415, in which three pairs of mode numbers of (l, n) = (1,999), (1,991), and (1,1001), are utilized to identify the distribution of WGMs, respectively. Figures 4(a)-(c) display the radial field intensity distributions, which indicate that higher n_2 lead to deeper EW penetration and larger η. The corresponding η values are 0.041, 0.097, and 0.149, respectively. The lasing feedback mechanism of a FOFL varying with n_2 is also analyzed using the finite element method. Figures 4(d)-(f) illustrate the optical field distribution for various n_2 within the WGM plane, each exhibiting a distinct bright ring. Enlarging the dotted rectangular regions in these figures, the respective detailed field distributions are revealed in the inset of Figs. 4(d)-(f), respectively. Notably, light to dark modes in the optical field are distinctly observable at the fiber-liquid interface. The majority of energy is confined within the fiber, with a smaller portion forming an EW outside. Furthermore, the EW penetration depth is observed to increase with increasing n_2 (inset of Figs. 4(d)-(f)), resulting in a continuous increase in parameter η.

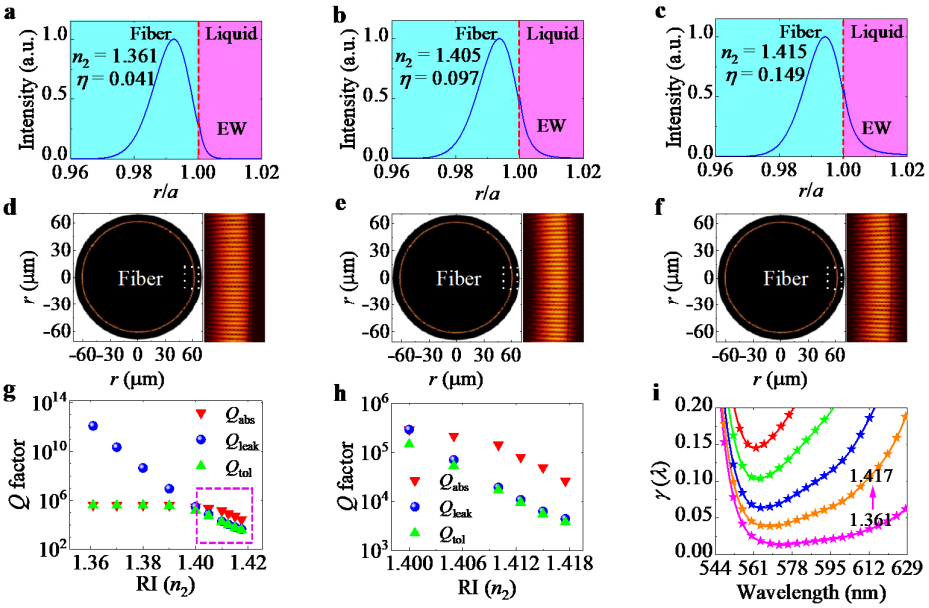

Fig. 4. (a)-(f) Modal distributions of transverse electric (TE) wave WGMs at n_2 values of 1.361, 1.405, and 1.415, with (l, n) = (1,999), (1,991), and (1,1001), respectively. (a)-(c) Radial field intensity distributions. (d)-(f) Optical field distributions in the WGM plane using the finite element method. The right insets show the enlarged views of the dotted rectangles in Figure (d)-(f). (g) Q-factor as a function of n_2. (h) The enlarged views of the pink dotted rectangle in Figure (g). (i) γ(λ) depicts the fraction of excited molecules at the lasing threshold for different n_2 values.

Let Q_{abs}, Q_{leak}, and Q_{sca} represent the Q-factors of a FOFL due to the energy losses from absorption (α_{abs}), leakage (α_{leak}), and scattering (α_{sca}), respectively. The total Q (Q_{tol}) of a WGM can be written as $Q_{tol}^{-1} = Q_{abs}^{-1} + Q_{leak}^{-1} + Q_{sca}^{-1}$. Figure S2(a) (Supplement 1) presents an

Optics EXPRESS

AFM image of the fiber surface with a roughness of ~ 0.7 nm, resulting in a $Q_{sca} \sim 4 \times 10^{11}$, which is negligible compared to Q_{abs} (~10^5-10^6) (Fig. 4(g)). Thus, the Q_{tol} is approximated to $Q_{tol}^{-1} \approx Q_{abs}^{-1} + Q_{leak}^{-1}$. As shown in Fig. 4(g), for n_2 values before the IP (1.400), the Q_{tol} of the resonator is mainly determined by Q_{abs}, decreasing slightly from ~4×10^5 to 3×10^5. After the IP, the increasing energy losses force the Q_{tol} to shift from being influenced by both Q_{abs} and Q_{leak} to relying only on Q_{leak}, as shown in Fig. 4(h). This transition leads to a sharp drop in the Q_{tol} by about two orders of magnitude, from 3×10^5 to 3.8×10^3. Figs. S2(b)-(f) (Supplement 1) illustrates the calculated Q-factors versus n_2 for various optical fiber diameters. For the 100 (200) μm fiber, the Q-factor behaves like that of 125 μm fiber, as shown in Figs. S2(c) and S2(e) (Supplement 1). However, for the fiber with a 49 (400) μm diameter, the Q_{tol} is primarily determined by Q_{leak} (Q_{abs}) across the measured RI range (Figs. S2(b) and S2(f)).

According to the lasing theory, an FOFL will be lasing at λ where γ(λ) meets the laser threshold, which can be written as [31]

$$\gamma(\lambda) = \frac{\sigma_a(\lambda)}{\sigma_e(\lambda) + \sigma_a(\lambda)} \left(1 + \frac{Q_{abs}}{Q_{tol}}\right), \tag{3}$$

where σ_e (σ_a) is the emission (absorption) cross section at the lasing wavelength (λ).

Figure 4(i) illustrates the calculated γ(λ) for a diameter of 125 μm fiber across various n_2. For n_2 below the IP, the γ(λ) function is primarily influenced by σ_a and σ_e, both of which undergo a redshift, as shown in Fig. S3(c) (Supplement 1). However, for n_2 exceeding the IP, the Q_{tol} transforms co-determination of both Q_{abs} and Q_{leak} to eventually depend exclusively on Q_{leak}. Then, the wavelength at minimum γ(λ) continuously shifts to blue as n_2 increases, matching the experimental results in Fig. 2(d).

3.5. Combined effects on sensitivity

For clarity, the lasing central wavelength varied with n_2 is further subdivided into five stages (Figs. 5(a)-(e)): I rapid initial redshift, II slower redshift, III stabilization, IV gradual blueshift, and V accelerating blueshift. Due to the Q-factor (solvent effects) constraint, the fiber with a diameter of 49 (400) μm is restricted to stages IV and V (I and II), as shown in Figs. 5(d) and 5(e). It should be noted that fibers with different diameters have different n_2 ranges in each stage. Figure 5(f) illustrates the RI sensitivity for each stage: 170-180 nm/RIU (I), 90-105 nm/RIU (II), 0.6-3 nm/RIU (III), 260-280 nm/RIU (IV), and 1013-1058 nm/RIU (V). Obviously, the sensitivity undergoes an initial decline followed by an increase from stage I to V.

We propose that the sensitivity variations across different stages result from the combined interaction between the polar-induced solvent effect and the fluctuations in the RI-induced Q-factor of the resonator. Before stage III, the EW penetration depth is small ($0.013 < \eta < 0.08$) (I-II area in Fig. 5(g)), yielding a relatively high Q-factor predominantly governed by absorption losses ($3.2 \times 10^5 < Q_{tol} < 1.4 \times 10^6$) (I-II area in Fig. 5(h)). Consequently, the impact of the solvent effect on the lasing wavelength substantially surpasses the reduction in the Q-factor (*i.e.*, increase in energy losses), causing a redshift in the lasing wavelength as n_2 (solvent polarity) increases. Furthermore, the enhanced absorption loss associated with increasing n_2 also constrains the redshift in the lasing wavelength induced by the solvent effect, which results in a reduced RI sensitivity in stage II compared to stage I. At stage III, characterized by a η (Q_{tol}) value of approximately 0.08 (3.2×10^5), the combined effect of the solvent effect and absorption loss on the lasing wavelength balances out, thereby yielding a minimal sensitivity. However, after stage III, the η value rises from 0.08 to ~0.134 (III area in Fig. 5(g)) in stage IV due to the increasing n_2. Consequently, the Q_{tol} transitions to being determined by both absorption and light leakage losses in stage IV ($1.2 \times 10^4 < Q_{tol} < 3.2 \times 10^5$) (III area in Fig. 5(h)). At this stage, the influence of the Q-factor on the lasing wavelength begins to exceed that of the solvent effect, resulting in a blueshift in the lasing wavelength with a sensitivity of ~260 nm/RIU to 280 nm/RIU. Upon

Optics EXPRESS

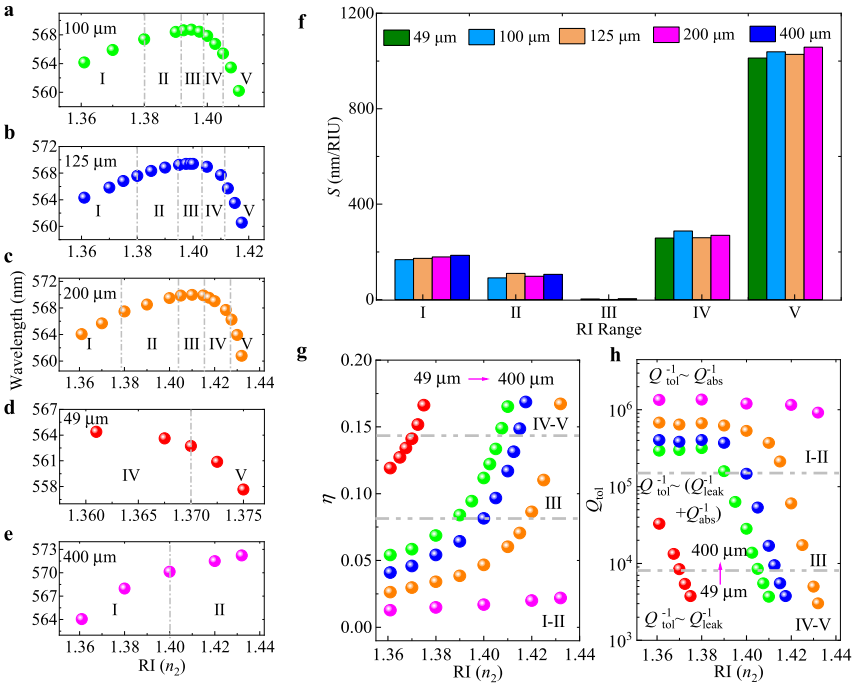

Fig. 5. (a)-(e) Lasing central wavelength for different fibers varied across five stages with n_2, I: rapid initial redshift, II: slower redshift, III: stabilization, IV: gradual blue shift, and V: accelerating blueshift. (f) Sensitivity in each stage. (g) η and (h) Q-factors varied with n_2 across different fibers and experimental stages.

further increasing n_2 to stage V, the η value increases to ~0.18 (IV-V area in Fig. 5(g)). Then, the energy loss is mainly due to the light leakage ($2.1 \times 10^3 < Q_{tol} < 1.2 \times 10^4$) (IV-V area in Fig. 5(h)), which affects the lasing wavelength significantly more than the solvent effect. Consequently, the sharply reduced Q-factor at this stage results in extremely high sensitivity, around 1013 nm/RIU-1058 nm/RIU.

We additionally perform a comparative analysis to evaluate the sensitivity in DI water and in EtOH and EG binary solvents, respectively. The lasing central wavelength as a function of n_2 illustrated in Fig. 3(f) is also categorized into five distinct stages, as demonstrated in Fig. S5 (Supplement 1). In the first three stages, the energy losses of the resonator are primarily driven by absorption. Consequently, the sensitivity in DI water is nearly zero, much lower than in EtOH & EG, as shown in Fig. 6(a). However, in stages IV and V, the energy losses of the resonator increase with increasing n_2, which experiences a shift from being affected by both absorption and leakage to being dominated only by light leakage. Then, the sensitivity in aqueous solution rises to ~310 nm/RIU (stage IV) and 1206 nm/RIU (stage V), increasing by ~50 nm/RIU and 180 nm/RIU compared to the EtOH and EG mixed solvent.

3.6. *Framework of Q-factor levels on sensitivity*

As mentioned above, the sensitivity of a FOFL sensor is strongly influenced by both the evanescent field penetration depth and the Q-factor of the resonator. However, it should be noted that it is difficult to independently evaluate the effects of η and Q-factor on the laser performance and sensitivity in practical applications. Instead, using the effective Q ($Q_{eff} = \eta Q_{tol}$) allows for a

Optics EXPRESS

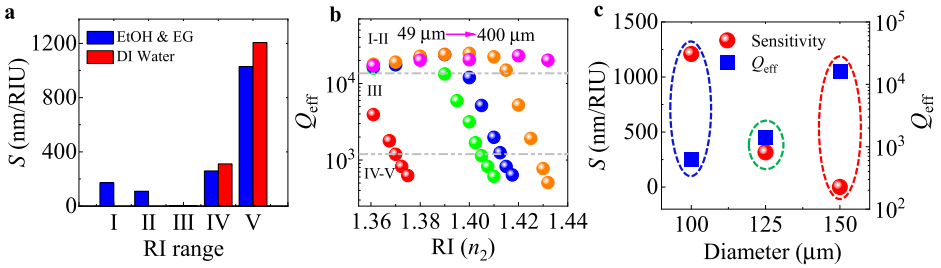

Fig. 6. (a) Sensitivity comparison of 125 μm fiber in DI water versus in EtOH & EG mixed solution. (b) Effective Q (Q_{eff}) varied with n_2 across various fiber diameters at different stages. (c) Sensitivity (S) and Q_{eff} varied with fiber diameter for n_2 values between 1.395 and 1.405.

better analysis of the interaction between the EW and the gain medium, and its impact on the sensing sensitivity.

Figure 6(b) can be regarded as a general framework for predicting the RI sensitivity of a WGM laser sensor at different Q_{eff} factor levels within a single solvent. Specifically, when the Q_{eff} is above 1.6×10^4 (I-II region), the lasing wavelength exhibits insensitivity to RI changes. In the range of 1.2×10^3 to 1.6×10^4 (III region), the sensitivity increases significantly. Below 1.2×10^3 (IV-V region), the lasing wavelength demonstrates the highest sensitivity to RI changes. We initially consider the aqueous solution depicted in Fig. 6(a) as an illustrative example. In stages I to III, the Q_{eff} value is over 1.6×10^4, yielding a sensitivity of ~0 nm/RIU. In stage IV, the Q_{eff} value drops to 1.7×10^3, increasing sensitivity to 310 nm/RIU. By stage V, the Q_{eff} decreases to $\sim8\times10^2$, at which point the sensitivity is as high as ~1200 nm/RIU. We also quantified the sensitivity of various optical fibers for the aqueous solution within the n_2 range of 1.395-1.405 using the Q_{eff} value. Figure 6(c) shows that the 150 μm fiber has a Q_{eff} exceeding 1.6×10^4, indicating the lowest sensitivity (red dotted box). The 125 μm fiber has a Q_{eff} value of $\sim 1.4\times10^3$ and a sensitivity of up to 315 nm/RIU (green dotted box), whereas the 100 μm fiber has the lowest Q_{eff} value of 6.2×10^2 but the highest sensitivity of ~1200 nm/RIU (blue dotted box).

4. Conclusion

In conclusion, we have demonstrated the influence of solvent polarity and RI on the performance of a FOFL sensor. As the RI of the binary polarity solvent increases, two competing phenomena are observed: increasing solvent polarity can induce a redshift in the lasing wavelength, whereas substantial drop in the Q-factor with increasing RI results in a blueshift. The interaction of these two opposing effects substantially decreases the sensitivity of the sensor. By selecting a single gain medium solvent (such as aqueous solution), the lasing wavelength shift attributed to the solvent effect can be effectively eliminated, thereby significantly enhancing the sensitivity associated with the blueshift. This study demonstrates that an increase in the solution RI results in a higher mode volume ratio η and a lower Q-factor, which together enhance sensing sensitivity. Based on those findings, we offer a comprehensive framework for predicting the sensitivity of WGM laser sensors across varying Q-factor levels. We expect that this study can provide valuable guidelines for optimizing the design and fabrication of WGM laser sensors. In addition, the proposed WGM sensor is applicable to the highly sensitive detection of component concentrations in mixed solvents with different polarities. For instance, by exploiting the polarity difference between water and EtOH, the system can be utilized to detect the water content in EtOH. Additionally, EG, as a hygroscopic substance, can be employed with this system for humidity detection, based on its polarity contrast with water.

Optics EXPRESS

Funding. National Natural Science Foundation of China (12404443); Natural Science Foundation of Yunnan Province (202301BF070001-002); Xingdian Talents Program of Yunnan Province (YNWR-QNBJ-2019-149); China Scholarship Council (202307030044); Scientific Research Project of Postgraduate Students of Yunnan University (KC-23235352, KC-23235361); Caiyun Postdoctoral Project (C615300504057).

Disclosures. The authors declare no conflicts of interest.

Data availability. Data underlying the results presented in this paper are not publicly available at this time but may be obtained from the authors upon reasonable request.

Supplemental document. See Supplement 1 for supporting content.

References

1. S. Yang, Y. Wang, and H. Sun, "Advances and prospects for whispering gallery mode microcavities," Adv. Opt. Mater. **3**(9), 1136–1162 (2015).
2. D. Yu, M. Humar, K. Meserve, *et al.*, "Whispering-gallery-mode sensors for biological and physical sensing," Nat. Rev. Methods Primers **1**, 83 (2021).
3. Y. Zheng, Z. Wu, P. Ping Shum, *et al.*, "Sensing and lasing applications of whispering gallery mode microresonators," Opto-Electron. Adv. **1**(9), 18001501 (2018).
4. N. Toropov, G. Cabello, M. P. Serrano, *et al.*, "Review of biosensing with whispering-gallery mode lasers," Light: Sci. Appl. **10**(1), 42 (2021).
5. X. Wu, M. K. K. Oo, K. Reddy, *et al.*, "Optofluidic laser for dual-mode sensitive biomolecular detection with a large dynamic range," Nat. Commun. **5**(1), 3779 (2014).
6. Y.-C. Chen, Q. Chen, and X. Fan, "Lasing in blood," Optica **3**(8), 809 (2016).
7. H. Zhang, Y. Zhang, L. Li, *et al.*, "Optofluidic lasers and their applications in biochemical sensing," Lab Chip **23**(13), 2959–2989 (2023).
8. Z. Xu, Y. Yan, X. Wang, *et al.*, "Determination of enantiomeric excess by optofluidic microlaser near exceptional point," Adv. Sci. **11**(7), 2308362 (2024).
9. X. Yang, C. Gong, C. Zhang, *et al.*, "Fiber optofluidic microlasers: structures, characteristics, and applications," Laser Photonics Rev. **16**(1), 2100171 (2022).
10. D. Li, Q. Xu, F. Zhao, *et al.*, "Highly sensitive and selective detection of nitrite using a fiber optofluidic laser," Opt. Express **31**(20), 31982–31992 (2023).
11. D. Li, L. Zhou, Q. Yu, *et al.*, "Optical fiber optofluidic laser based on surfactant solubilization of rhodamine B gain in an aqueous solution," Opt. Express **30**(13), 23295–23304 (2022).
12. S. Subramanian, H. Wu, T. Constant, *et al.*, "Label-free optical single-molecule micro- and nanosensors," Adv. Mater. **30**(51), 1801246 (2018).
13. Z. Yuan, X. Cheng, Y. Zhou, *et al.*, "Distinguishing small molecules in microcavity with molecular laser polarization," ACS Photonics **7**(8), 1908–1914 (2020).
14. X. Jiang, A. J. Qavi, S. H. Huang, *et al.*, "Whispering-gallery sensors," Matter **3**(2), 371–392 (2020).
15. F. Vollmer and S. Arnold, "Whispering-gallery-mode biosensing: label-free detection down to single molecules," Nat. Methods **5**(7), 591–596 (2008).
16. J. Liao and L. Yang, "Optical whispering-gallery mode barcodes for high-precision and wide-range temperature measurements," Light: Sci. Appl. **10**(1), 32 (2021).
17. Y. Wang, S. Zeng, G. Humbert, *et al.*, "Microfluidic whispering gallery mode optical sensors for biological applications," Laser Photonics Rev. **14**(12), 2000135 (2020).
18. Z. Wang, T. Xu, A. Noel, *et al.*, "Applications of liquid crystals in biosensing," Soft Matter **17**(18), 4675–4702 (2021).
19. Z. Li, D. Li, M. Zhang, *et al.*, "Large dynamic range dual-mode ph sensors via dye-doped ionic liquid fiber optofluidic lasers," Analyst **148**(20), 5050–5059 (2023).
20. D. Li, M. Zhang, L. Zhou, *et al.*, "Monitoring the pH Value of an Aqueous Micellar Solution in Real-Time Using a Fiber Optofluidic Laser," J. Lightwave Technol. **41**(1), 362–366 (2023).
21. S. Zhang, N. Liang, X. Shi, *et al.*, "Direction-adjustable single-mode lasing via self-assembly 3D-curved microcavities for gas sensing," ACS Appl. Mater. Interfaces **13**(38), 45916–45923 (2021).
22. Y. Xu, P. Bai, X. Zhou, *et al.*, "Optical refractive index sensors with plasmonic and photonic structures: promising and inconvenient truth," Adv. Opt. Mater. **7**(9), 1801433 (2019).
23. P. Ji, M. Zhu, C. Liao, *et al.*, "In-fiber polymer microdisk resonator and its sensing applications of temperature and humidity," ACS Appl. Mater. Interfaces **13**(40), 48119–48126 (2021).
24. E. Kim, M. D. Baaske, and F. Vollmer, "Towards next-generation label-free biosensors: recent advances in whispering gallery mode sensors," Lab Chip **17**(7), 1190–1205 (2017).
25. A. Shevchenko, K. Lindfors, S. Buchter, *et al.*, "Evanescent-wave pumped cylindrical microcavity laser with intense output radiation," Opt. Commun. **245**(1-6), 349–353 (2005).
26. X. Jiang, Q. Song, L. Xu, *et al.*, "Microfiber knot dye laser based on the evanescent-wave-coupled gain," Appl. Phys. Lett. **90**(23), 233501 (2007).

Optics EXPRESS

27. I. Aburto, M. Muñoz, M. Vidal, *et al.*, "Extending the π-system of inverted solvatochromic phenolate-based dyes shifts their inversion point due to an increment in their sensitivity to Solvent Polarizability," J. Mol. Liq. **368**, 120784 (2022).
28. A. Gregory and R. Clarke, "Traceable measurements of the static permittivity of dielectric reference liquids over the temperature range 5–50∘C," Meas. Sci. Technol. **16**(7), 1506–1516 (2005).
29. V. Divac, D. Sakic, T. Weitner, *et al.*, "Solvent effects on the absorption and fluorescence spectra of zaleplon: determination of ground and excited state dipole moments," Spectrochim. Acta, Part A **212**, 356–362 (2019).
30. A. Krishnamoorthy, K. Nomura, N. Baradwaj, *et al.*, "Dielectric constant of liquid water determined with neural network quantum molecular dynamics," Phys. Rev. Lett. **126**(21), 216403 (2021).
31. H. Zhang, A. Balram, D. Meng, *et al.*, "Optofluidic lasers with monolayer gain at the liquid−liquid interface," ACS Photonics **4**(3), 621–625 (2017).